

**Fig. 1** The molecular beam apparatus employed for the cluster synthesis and SID experiments in a schematic representation. The dashed line indicates the cluster ion trajectories in the time-of-flight mass spectrometer up to the electrostatic ion mirror (in position A) and the deflection directly onto the detector (low resolution mode, see text). Higher mass resolution can be obtained by using the mass reflectron. The ion trajectories behind the electrostatic mirror (rotated to position B) are indicated by the dashed-dotted line for this particular case. For the surface scattering experiment, the ions are deflected by the mirror (in position B) toward the target substrate and fragment ions are analyzed by their flight time from the surface to the detector (dotted line). The insert shows an enlarged view of the surface scattering assembly. The attached surface preparation UHV chamber is not shown here.

first chamber, which is pumped by two turbomolecular pumps with  $1000 \text{ l s}^{-1}$  capacity each. The second chamber with the ion acceleration electrodes is evacuated by another  $1000 \text{ l s}^{-1}$  turbomolecular pump and the third, surface scattering arrangement and detector chamber is pumped by a  $600 \text{ l s}^{-1}$  turbomolecular pump. Base pressure in all chambers is  $1 \times 10^{-10}$  mbar, the pressure during operation of the source never exceeds  $1 \times 10^{-7}$  mbar in the surface region and is solely due to the seed gas used for cluster production (He, 99.9999% purity). Further ultra high vacuum (UHV) chambers, which are not shown here, are attached to the surface scattering arrangement for convenient surface preparation and analysis.<sup>18</sup>

Particularly important for the present experiment is the electrostatic ion mirror in the third chamber. By rotating this mirror and by switching the electric field, the molecular ion beam can be deflected in either of three directions and the arrangement operates accordingly as: (i) simple time-of-flight mass spectrometer; (ii) as high resolution reflectron mass spectrometer; or (iii) as mass-selected, surface scattering and fragment ion detection spectrometer

#### A. Cluster ion source

Cluster ions were directly generated by a gas discharge ion source, which is shown schematically in Fig. 2. Helium gas with a backing pressure of up to 20 bar is pulsed between two electrodes by a commercial solenoid valve (General valve Ser. 9). Correlated with the He gas pulse, a high voltage pulse (up to 1 kV) is applied to the electrodes and thus a discharge lasting several tens of microseconds is generated. In the course of the discharge electrode material is evaporated or sputtered from the cathode. A plasma is generated consisting of rare gas ions, electrons and metal ions. This plasma flows through the nozzle channel (length: up to 80 mm, diameter 1 to 3 mm) to enhance cluster formation and is finally expanded into the vacuum. The energy for the gas discharge is delivered by high

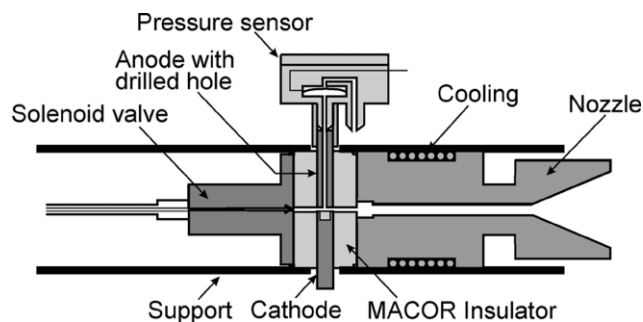


**Fig. 2** Schematic drawing of the pulsed discharge cluster ion source. The cylindrical molybdenum electrodes (5 mm diameter) are mounted in a  $40 \times 40 \times 20$  mm MACOR insulator block which has a center channel with rectangular cross section of  $5 \times 1$  mm. For adjustment of the appropriate timing between valve opening and discharge ignition the gas pressure inside the source can be monitored via a miniature pressure sensor (Sensortronics, Puchheim, Germany) attached to the bored anode.

voltage capacitors with capacities between 10 and  $40 \mu\text{F}$ . For optimal timing control between discharge and gas pulse, the gas pressure inside the source is monitored with a miniature semiconductor pressure sensor,<sup>19</sup> which is directly connected to the inside of the source, *i.e.* the discharge region, by a hole drilled into the anode (Fig. 2). We used high purity (99.9999%) helium carrier gas in order to avoid the presence of trace amounts of oxygen and water, since these lead instantly to the formation of oxides and hydroxides.<sup>20</sup> The antimony and bismuth samples were of 99.999% purity (Alfa/Johnson Matthey). These materials were mechanically pressed into a hole in the molybdenum cathode (molybdenum > 99.9% purity, Alfa/Johnson Matthey).

#### B. Time-of-flight mass spectrometer

The mass spectrometer is aligned with the molecular beam emerging from the discharge source. After passing the skimmer, the ions are accelerated by a two stage Wiley/McLaren type field.<sup>21</sup> The beam can be focused by a single einzel lens in the field free drift path. The third chamber contains the specially designed ion mirror. It consists of two stainless steel meshes with 90% transmission. One mesh is always on ground potential and a high voltage pulse is applied to the second one. The ion mirror is set up in such a way that it can be rotated by 360 degree during the experiment. If the mirror is in position A (Fig. 1) and on high constant potential, the ions are directly deflected onto a chevron dual multichannel plate (MCP) detector. In this mode the mass resolution is  $m/\Delta m = 85$ . Mass-selection is achieved by the application of a high voltage pulse, which is timed to allow only the ion packet with the mass-to-charge ratio of interest to pass the mirror in the direction of the detector.

In order to obtain a higher mass resolution a double field reflectron has been added to the apparatus.<sup>22,23</sup> In the reflectron mode (Position B, Fig. 1), the accelerated ions first pass the grounded mirror and are subsequently reflected. The reflected ions arrive again at the mirror, which has been switched to a high potential in the meantime, and are deflected toward the detector. The mass resolution achieved in this reflectron mode is  $m/\Delta m = 400$ .

If the mirror is rotated by  $90^\circ$  to position B, the cluster ions are directed onto the substrate surface, which is located directly opposite the detector and SID spectra can be recorded.

#### C. Surface scattering experiment

In most of the experiments presented here highly oriented pyrolytic graphite (HOPG) was employed as substrate material. The graphite(0001) basal plane is a well defined, inert, and easy

to prepare surface. The samples were cleaved in air prior to their installation into the vacuum chamber. In this way an atomically flat (0001) surface can be obtained. Further cleaning is achieved by heating the substrate to 600 °C in UHV for several hours.<sup>24</sup>

The cluster ions were also scattered from a Si(001) surface. This surface is used with the naturally present thin surface oxide layer, which reduces the reactivity of the uncovered silicon surface and also increases the surface electron binding energy, thus reducing neutralization probability of the colliding cluster ions. Scattering from this surface therefore leads to an increased scattered ion yield as will be shown below. We employed a boron p-doped silicon wafer disk, which was cleaned by heating to 600 °C in UHV.

The third substrate, which was used for the SID of selected antimony cluster ions, was a metallic gold sample. A well defined Au(111) surface with atomically flat areas of the size of over 1000 nm<sup>2</sup> was prepared by deposition of a *ca.* 200 nm thick gold film onto a 150 µm thick Mica sheet.<sup>25</sup> These samples were cleaned immediately before their insertion into the vacuum chamber by flame-annealing, *i.e.* heating to a red glow with a butane flame for about one second. Further cleaning was achieved by heating in vacuum to 400 °C, in order to remove water traces.

Following preparation, the substrate is transferred to the scattering assembly inside the vacuum chamber without breaking vacuum by rotation/translation feedthroughs. The substrate surface is positioned directly opposite the ion detector, at the same distance from the electrostatic mirror as the detector (Fig. 1). If the mirror is rotated to position B, the ions are focused onto the substrate surface. Ions and fragment ions, which are reflected or scattered from the surface, are then accelerated along the surface normal toward the detector. After passage of the mirror, which has been switched to ground potential in the meantime, they reach the MCPs and are detected with flight times according to their mass-to-charge ratio.

The insert of Fig. 1 shows an enlarged view of the surface scattering setup. The substrate holder is pushed against a copper electrode inside the scattering assembly. The copper electrode is mounted inside a liquid nitrogen cryostat to allow the variation of surface temperature. The experiments presented here were all carried out at room temperature. The incident cluster ions are decelerated in front of the surface by the high bias voltage applied to the substrate. In addition, an einzel lens arrangement is mounted in front of the deceleration field to focus the cluster beam onto the surface. A surface collision takes place, if the surface potential is lower than the maximum beam energy given by the acceleration voltage.

The energy width of the cluster ion beam can be reduced efficiently in our setup by an appropriate delayed pulsing of the acceleration fields of the mass spectrometer.<sup>26</sup> The energy width in the experiments presented here was chosen to be between ±20 and ±50 eV, according to the intensity requirements for the incident cluster ion beam.

### III. Results and discussion

#### A. Structure and stability of antimony and bismuth clusters

In this section we will first briefly review known data about the structure and energetics of antimony and bismuth clusters which are essential to the understanding of the measured mass spectra and stability patterns. The gas phase of antimony consists over a broad temperature range exclusively of the tetramer Sb<sub>4</sub>.<sup>27</sup> This cluster has a tetrahedral structure<sup>28–30</sup> and a relatively high total binding energy of 8.9 eV.<sup>31</sup> The energy necessary for the dissociation of Sb<sub>4</sub> in two Sb<sub>2</sub> molecules has been reported to be 2.86 eV<sup>31</sup> or 2.5 eV.<sup>32</sup> The binding

energy of Sb<sub>2</sub> has been measured to be 3.1 eV.<sup>31</sup> If antimony vapor is allowed to condense in a cooled gas aggregation cluster source, solely cluster species belonging to the series Sb<sub>4n</sub> (with  $n = 1, 2, 3, \dots \sim 160$ ) are observed.<sup>2</sup> It has been proposed that these clusters consist of a closest packing of Sb<sub>4</sub> units.<sup>9</sup> Structure models calculated using quantum chemical *ab initio* methods also indicate tetrameric subunits in the Sb<sub>4n</sub> series clusters.<sup>10,11</sup> The binding energy of Sb<sub>4</sub> units in Sb<sub>4n</sub> clusters ( $n = 2–5$ ) has been determined to be 1.3 eV.<sup>3</sup> This value is considerably less than the energy necessary to evaporate an Sb<sub>4</sub> cluster from a solid antimony surface which amounts to 2.15 eV.<sup>27,33</sup> A solid state modification of antimony consisting solely of Sb<sub>4</sub> clusters, analogous to the structure of white phosphorus (P<sub>4n</sub>) or yellow arsenic (As<sub>4n</sub>), has not been observed as bulk material<sup>6</sup> but might exist in thin films of antimony.<sup>34</sup> Further indication for the special geometric and electronic properties of the Sb<sub>4n</sub> clusters (with  $n > 1$ ) is also given by their inner shell photoionization spectra which are in striking difference to those of clusters not belonging to this series.<sup>35</sup>

The intensity distribution in a molecular beam of charged antimony clusters turns out to be very different from the neutral cluster distributions just described. The cluster cation distributions show intensity maxima for Sb<sub>3</sub><sup>+</sup>, Sb<sub>5</sub><sup>+</sup> and Sb<sub>7</sub><sup>+</sup>.<sup>36,37</sup> To explain these observations Wade's rules have been applied to these free semi-metal clusters.<sup>38,39</sup> According to Wade, a close connection exists between the number of valence electrons and the geometrical structure of clusters or molecules with electron deficiency. The Wade rules predict stability maxima for clusters with  $2n + 2$  (closo-cluster),  $2n + 4$  (nido-cluster), and  $2n + 6$  (arachno-cluster) valence electrons,  $n$  being the number of constituting atoms. They have been applied with great success to explain the structures of boranes. Using an extended approach, the so-called polyhedral skeletal electron pair theory (PSEPT),<sup>40,41</sup> they can also be applied to, *e.g.*, transition metal clusters.<sup>42</sup> The electron configuration of antimony is Kr 4d<sup>10</sup>5s<sup>2</sup>5p<sup>3</sup>. Hence, Sb<sub>3</sub><sup>+</sup> can be interpreted as a particular stable close-Wade-cluster, considering only the p-electrons. Sb<sub>5</sub><sup>+</sup> and Sb<sub>7</sub><sup>+</sup> are also stable compounds with nido- and arachno-structures, respectively.<sup>37</sup> It should be noted that Sb<sub>4</sub> has a particular high stability in the framework of the PSEPT, too. A mass spectrum of positively charged antimony cluster ions generated with our discharge cluster ion source is shown in Fig. 3(a). The abundance distribution shows intensity maxima for Sb<sub>3</sub><sup>+</sup>, Sb<sub>4</sub><sup>+</sup>, Sb<sub>5</sub><sup>+</sup>, and Sb<sub>7</sub><sup>+</sup>, in accordance with the above discussion. In addition, an intensity decrease after clusters with a multiple of four atoms is observed, too.

As bismuth is the next heavier homologous element to antimony, clusters of bismuth have the same valence electron structure as the antimony clusters (s<sup>2</sup>p<sup>3</sup>). It can therefore be expected that cluster cations with three, five, and seven atoms also show enhanced stability according to PSEPT, which is indeed reflected by the intensity distribution in the mass spectrum (Fig. 3(b)).

The gas phase above liquid bismuth consists mainly of Bi atoms and Bi<sub>2</sub> molecules with only trace amounts of Bi<sub>3</sub> and Bi<sub>4</sub> present.<sup>27,43,44</sup> In contrast to antimony, there is no indication of the particular stability of the tetrameric bismuth cluster. The total binding energies of the dimeric and tetrameric antimony and bismuth clusters are compared in Table 1. A 4n sequence in cluster mass spectra, comparable to the Sb<sub>4n</sub> series, has not been observed for bismuth clusters. Cluster distributions generated with a gas aggregation source contain all Bi<sub>n</sub> clusters with  $n \leq 280$  atoms.<sup>2–4,45</sup>

#### B. Surface induced dissociation of antimony and bismuth cluster ions

Fig. 4(a) shows the fragment ion mass spectra of Sb<sub>8</sub><sup>+</sup> after collision with different target surfaces in the collision energy

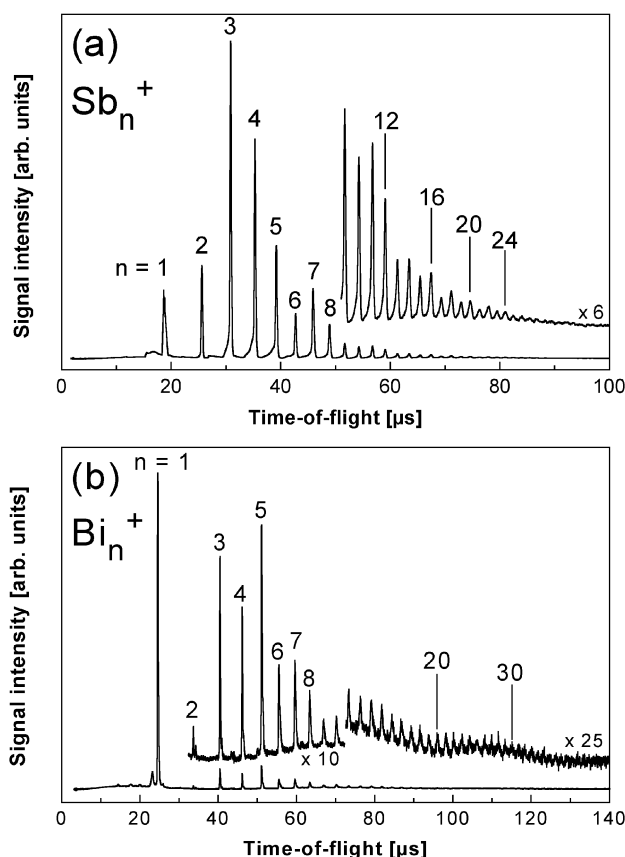
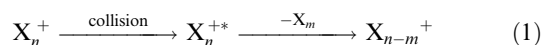


**Fig. 3** Mass spectra of the unscattered beam of (a) antimony and (b) bismuth clusters. Note that besides the enhanced peak intensities for the Wade-cluster cations with 3, 5 and 7 atoms, there is a marked abundance decrease after each  $\text{Sb}_n^+$  cluster with a multiple of four atoms ( $\text{Sb}_4^+$ ,  $\text{Sb}_8^+$ ,  $\text{Sb}_{12}^+$ , ...) which is not observed in the  $\text{Bi}_n^+$  cluster distribution

range up to 150 eV. As can be seen from these spectra, the major fragment,  $\text{Sb}_4^+$ , is the same for all three surfaces. In Fig. 4(b) the SID mass spectra of  $\text{Bi}_5^+$  are displayed. The fragment ion distributions are again similar for the two investigated surfaces up to a collision energy of 50 eV.  $\text{Bi}_3^+$  is the most abundant fragment ion. The result that the SID fragment ion pattern of a cluster ion is in general independent of the particular target (Au, HOPG, Si), at hyperthermal collision energies, could be confirmed for all antimony and bismuth clusters investigated. It implies that the decomposition mechanism is similar even for different surfaces.

The mechanism proposed in the literature<sup>46–49</sup> for the decomposition of a molecule or cluster  $\text{X}_n^+$  due to the low energy collision with a solid surface is the activation of the ion (\*) by vibrational excitation according to the general scheme:



The interaction time of the ions with the target surface during the collision is on the order of  $10^{-14}$  s, whereas the low energy dissociation reactions of polyatomic molecules or clusters proceed on a much longer timescale of  $> 10^{-9}$  s.<sup>48</sup> Hence,

**Table 1** Total binding energies  $E_B$  of the dimeric and tetrameric antimony and bismuth clusters

$n$	$E_B(\text{Sb}_n) [\text{eV}]^{31}$	$E_B(\text{Bi}_n) [\text{eV}]^{65}$
2	3.1	2.06
4	8.94	6.03

it can be assumed that the decomposition of an activated ion takes place some time after the collision.<sup>50</sup> By comparison with gas phase fragmentation data, we will show below that in the case of antimony and bismuth cluster cations scheme (1) corresponds to the lowest energy unimolecular dissociation reactions.

In the case of  $\text{Bi}_5^+$  colliding with the graphite target (Fig. 4(b)) additional smaller fragments appear above 75 eV collision energy. This indicates the onset of a new decomposition mechanism which is connected with the surface ionization of neutral fragments at the graphite substrate. This mechanism has been observed before at higher collision energies for  $\text{Sb}_n^+$  clusters.<sup>15</sup> It has been observed for  $\text{C}_{60}$  cluster collisions with graphite targets, too,<sup>51</sup> but will not be discussed in this paper.

Although the general fragment ion distributions for a colliding cluster ion as depicted in Fig. 4 do not change for the different surfaces employed, the intensity of the fragment signals, e.g.  $\text{Sb}_4^+$  in Fig. 4(a), relative to the intensity of the incident mother ion signal (as reflected by the signal at 0 eV collision energy) varies considerably for different target surfaces. In particular, collisions with the silicon surface lead to clearly enhanced fragment ion signal intensities. For the graphite surface scattered ion yields up to at most 30% of the colliding mother ion intensity have been measured, depending on the size and the energy of the colliding cluster (see section D). The integrated fragment ion signal scattered from a gold surface was found to be comparable to or slightly less than the graphite results. In contrast, a scattered ion yield of up to 90% was observed for the oxidized silicon surface. The relatively high scattered ion yield for this surface can be related to its insulator type electronic properties, whereas the much lower work functions of the graphite and gold surfaces facilitate the efficient neutralization of the colliding cluster ions. Surprisingly large ion scattering efficiencies have been reported for gold surfaces covered with SAMs (self assembled organic monolayers), too. The organic surface acts as an insulating layer, comparable to the silicon oxide surface layer, which inhibits charge transfer to the colliding ion, thus enhancing the scattered ion yield.<sup>50</sup>

In the following discussion the SID results for antimony and bismuth clusters will be compared to other gas phase fragmentation data, in order to elucidate the general decomposition reaction pathway after surface collisional excitation in the case of the semi-metal clusters. The results of the SID measurements reported in this paper can most likely be compared with fragment ion distributions resulting from the collision of the corresponding cluster ions with gas targets at low collision energies (LE-CID, low energy collision induced dissociation<sup>52</sup>), or with the metastable delayed fragmentation of previously excited clusters (MIKES, mass-analyzed ion kinetic energy spectrometry,<sup>52</sup> or laser induced evaporation<sup>53</sup>). In all these methods the dissociation reaction presumably proceeds on the potential energy surface of the electronic ground state after vibrational excitation.<sup>52</sup> Other gas phase dissociative probes such as high energy collision induced dissociation (HE-CID<sup>52</sup>) and photodissociation (PD<sup>54</sup>) lead to different, generally less well defined excitation mechanisms with strong involvement of electronically excited states<sup>49,52</sup> and are therefore not considered here.

In Fig. 5 the measured SID fragment ion distributions for  $\text{Sb}_n^+$  ( $n = 3–12$ ) and  $\text{Bi}_n^+$  ( $n = 3–8$ ) and the graphite target are displayed together with the available LE-CID, MIKES, and laser evaporation data from the literature.<sup>52,53</sup> Table 2 shows possible fragmentation reactions of the antimony clusters with up to 8 atoms. The known dissociation energies  $E_D$  of  $\text{Sb}_n^+$  clusters, which have been determined by electron impact mass spectrometry,<sup>31</sup> are listed in Table 2 as well as literature values for the sums of the enthalpies of formation of the fragments,  $\sum \Delta_f H$ .<sup>55</sup> The possible fragmentation reactions

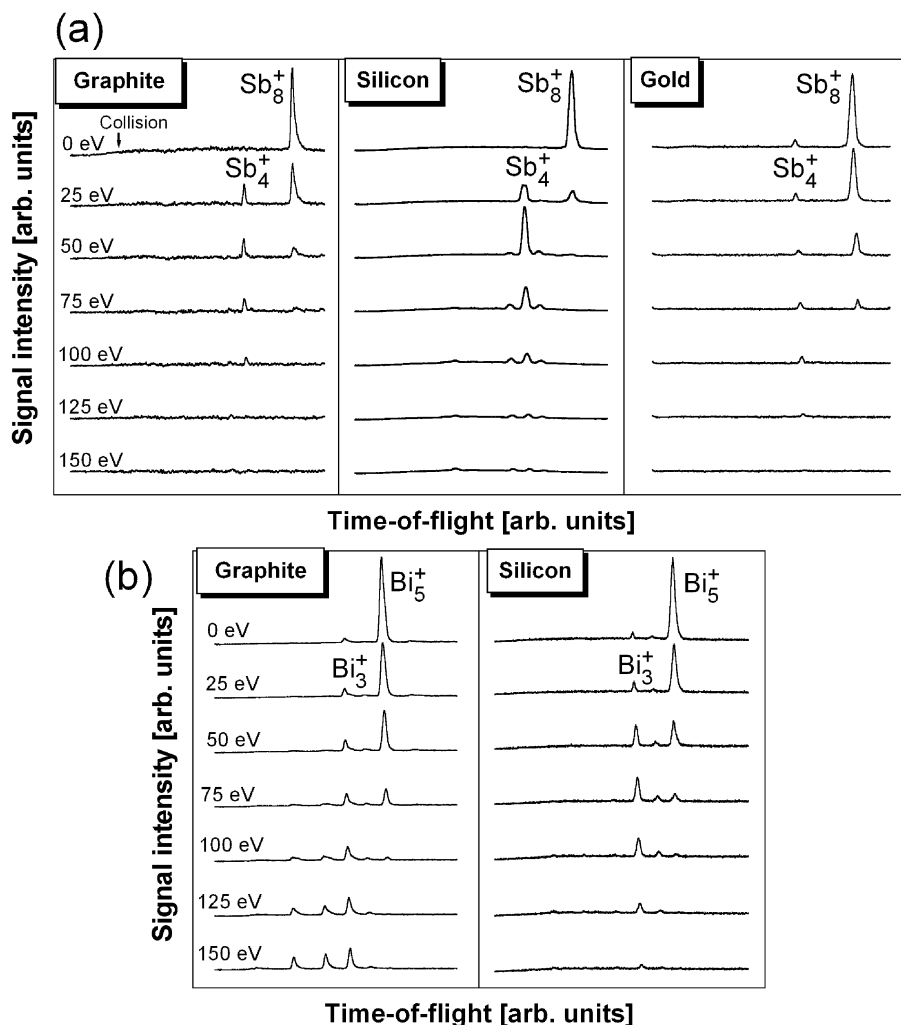


**Fig. 4** Fragment ion distributions for (a)  $\text{Sb}_8^+$  and (b)  $\text{Bi}_5^+$  scattered from various surfaces at collision energies up to 150 eV. The mother ion signal at the low collision energies results from back reflected clusters, which do not reach the surface, because of the width in kinetic energy of the incident cluster beam. Note that, although the most abundant fragments ( $\text{Sb}_4^+$  in (a) and  $\text{Bi}_3^+$  in (b)) are identical for different target surfaces, the intensities of the fragment ion signals relative to the mother ion signal intensity reflected at 0 eV vary considerably for the different surfaces. Additional peaks of smaller fragments ( $\text{Bi}^+$ ,  $\text{Bi}_2^+$ ) appearing in (b) at higher collision energies indicate the onset of a new decomposition mechanism,<sup>15,66</sup> see text.

for the bismuth clusters are analogous, however quantitative data for  $\text{Bi}_n^+$  cluster dissociation reactions are not available. In the following each cluster size will be discussed in turn.

In the case of surface induced dissociation of  $\text{Sb}_3^+$  the fragment ion  $\text{Sb}_2^+$  is generated (Fig. 5(a), left graph). The reaction leading to the observed fragment ion is highlighted in Table 2 by bold letters. The formation of  $\text{Sb}^+$  and two Sb atoms is energetically unfavorable (see Table 2). The observation of  $\text{Sb}_2^+ + \text{Sb}$  instead of  $\text{Sb}^+ + \text{Sb}_2$  can be explained by the difference in the ionization potentials (IP) of  $\text{Sb}_2$  and Sb:  $\text{IP}(\text{Sb}_2) = 8.5 \text{ eV} < \text{IP}(\text{Sb}) = 8.64 \text{ eV}$ .<sup>31,56</sup> The formation of  $\text{Sb}_2^+$  via the lowest energy unimolecular reaction channel is in accordance with all other fragmentation measurements reported in the literature (Fig. 5(a), right graph). For the surface induced dissociation of  $\text{Bi}_3^+$  both,  $\text{Bi}^+$  and  $\text{Bi}_2^+$  are detected (Fig. 5(b), left graph). Besides the unknown stability of the charged clusters, this might be due to different ionization potentials of  $\text{Bi}_2$  and Bi compared to  $\text{Sb}_2$  and Sb:  $\text{IP}(\text{Bi}_2) = 7.4 \text{ eV} > \text{IP}(\text{Bi}) = 7.29 \text{ eV}$ .<sup>3-5</sup> The LE-CID of  $\text{Bi}_3^+$  results in the fragment  $\text{Bi}^+$  (Fig. 5(b), right graph).

For the  $\text{Sb}_4^+$  cluster dissociation, the formation of  $\text{Sb}_3^+$  was found to be the predominant dissociation pathway (cf. Fig. 5(a)), which is again in accordance with the lowest energy dissociation channel (Table 2).  $\text{Sb}_3^+$  fragments were also the

exclusive products observed in the unimolecular gas phase dissociation of  $\text{Sb}_4^+$  in the MIKES and LE-CID experiments. The same applies to  $\text{Bi}_4^+$ , except that the smaller fragments ( $\text{Bi}_2^+$  and  $\text{Bi}^+$ ) appear to a larger extent than in the case of  $\text{Sb}_4^+$  which can be ascribed to the smaller total binding energy of the bismuth clusters as seen from Table 1.

Dissociation energies from electron impact mass spectrometry are not available for clusters with more than four atoms. In the case of  $\text{Sb}_5^+$ ,  $\sum \Delta_f H$  values have been determined for the dissociation reactions listed in Table 2. The SID result agrees with the previous investigations as shown in Fig. 5(a). All measurements point consistently toward the lowest energy unimolecular dissociation channel as the most prominent reaction path for the surface induced dissociation of  $\text{Sb}_5^+$ . This is the same again for  $\text{Bi}_5^+$ .

Also, for  $\text{Sb}_6^+$  the SID and laser evaporation data agree with the lowest energy unimolecular dissociation reaction according to the thermochemical data in Table 2. SID of  $\text{Sb}_6^+$ , as well as of  $\text{Sb}_5^+$ , shows the loss of neutral antimony dimers as the preferred dissociation channel (dashed line in Fig. 5(a)). The observed major SID fragment ion of  $\text{Bi}_6^+$  is similar to  $\text{Sb}_6^+$ , the tetrameric cluster ( $\text{Bi}_4^+$ ). However, LE-CID and MIKES result in  $\text{Bi}_5^+$  as lowest energy dissociation fragment ion of  $\text{Bi}_6^+$ . The  $\text{Bi}_5^+$  fragment is also detected in

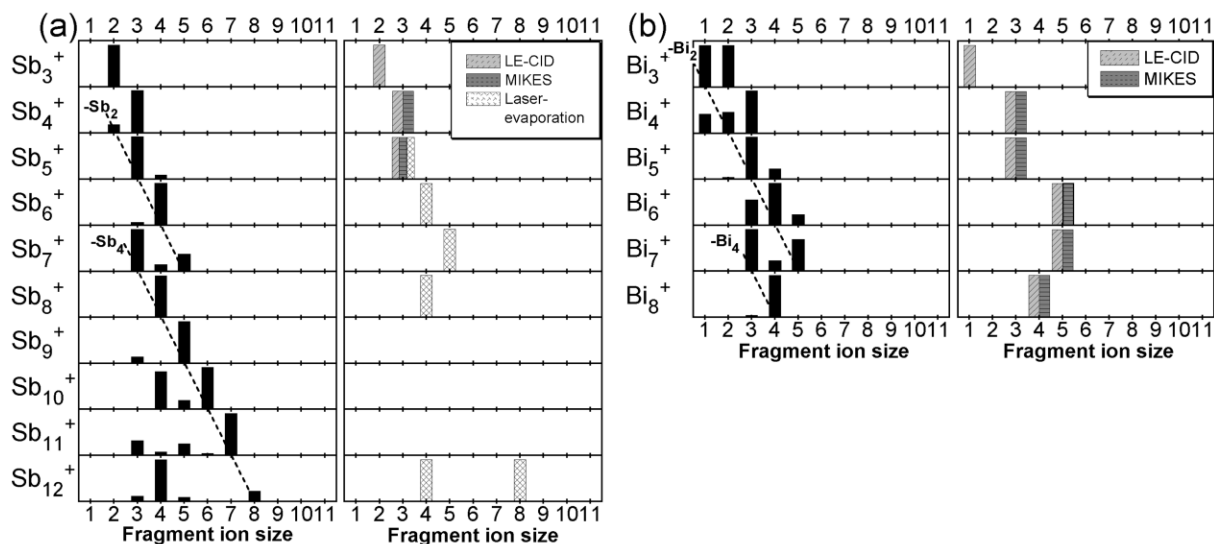
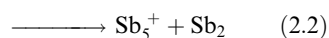


**Fig. 5** SID fragment ion distributions of all investigated cluster ions at a mean collision energy of 75 eV for the antimony clusters (a) and 25 eV for the bismuth clusters (b). Target surface: graphite. The dashed lines indicate the fragment ions which are generated by the loss of neutral dimers or tetramers, respectively. The fragment ion distributions are displayed as column graphs. The height of each column represents the integral of the respective fragment ion signal. Each fragment ion mass spectrum is normalized to the intensity of the most abundant fragment. This representation enables a convenient comparison of our results with fragment ion distributions obtained with other methods, which have been reported in the literature as numerical values, and which are displayed on the right hand side of (a) and (b), respectively. LE-CID: low energy collision with argon gas.<sup>52</sup> MIKES: mass analyzed ion kinetic energy spectroscopy.<sup>52</sup> Laser-evaporation: unimolecular dissociation after laser excitation.<sup>53</sup>

our SID experiment, but with lower intensity. This might be due to the particularly weak binding energy of  $\text{Bi}_6^+$  compared to the amount of energy transferred to the cluster at the collision energy given in Fig. 5(b).

From Fig. 5(a) it can be seen that for  $\text{Sb}_7^+$  the most abundant fragment ion results from a loss of four neutral antimony atoms which points toward reaction (2.1).

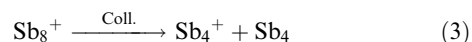


The unimolecular dissociation of metastable  $\text{Sb}_7^+$  clusters after laser excitation<sup>53</sup> (Fig. 5(a), right graph) implicates that the loss of  $\text{Sb}_2$ , as in the case of  $\text{Sb}_5^+$  and  $\text{Sb}_6^+$ , is in fact the lowest energy dissociation channel (reaction (2.2)). Apparently a transition is taking place at this cluster size: from the loss of neutral dimers to the loss of stable neutral tetramers. Such a transition has been suggested from the laser evaporation experiment, too.<sup>53</sup> For clusters with seven atoms no data about dissociation energies or enthalpies of formation are available.

**Table 2** Energies for the decomposition of  $\text{Sb}_n^+$  clusters

$X_n^+ \xrightarrow{\text{collision}}$	$X_{n-m}^+$	$X_m$	$E_D[\text{eV}]^{3,31}$	$\sum \Delta_f H [\text{eV}]^{55}$
$\text{Sb}_3^+$	$\text{Sb}_2^+$	Sb	$4.2 \pm 0.4$	
	$\text{Sb}^+$	$\text{Sb}_2$		
$\text{Sb}_4^+$	$\text{Sb}^+$	$2\text{Sb}$	$7.3 \pm 0.4$	
	$\text{Sb}_3^+$	Sb	$2.70 \pm 0.16$	2.21
	$\text{Sb}_2^+$	$\text{Sb}_2$	$3.80 \pm 0.12$	3.43
$\text{Sb}_5^+$	$\text{Sb}^+$	$3 \text{ Sb}$	$9.92 \pm 0.12$	
	$\text{Sb}_3^+$	$\text{Sb}_2$		9.87
	$\text{Sb}_4^+$	Sb		10.08
	$\text{Sb}_2^+$	$\text{Sb}_3$		11.14
$\text{Sb}_6^+$	$\text{Sb}^+$	$\text{Sb}_4$		11.60
	$\text{Sb}_4^+$	$\text{Sb}_2$	9.87	
	$\text{Sb}_3^+$	$\text{Sb}_3$		10.23
	$\text{Sb}_2^+$	$\text{Sb}_4$		11.07
$\text{Sb}_8^+$	$\text{Sb}_4^+$	$\text{Sb}_4$	1.3	

$\text{Sb}_4^+$  is the only fragment of  $\text{Sb}_8^+$  at low collision energy, which is in accordance with the unimolecular decomposition of excited, metastable  $\text{Sb}_8^+$  clusters.<sup>53</sup> Therefore it can be assumed that the unimolecular dissociation reaction (3) leads to the observed fragment ion.



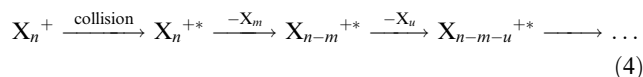
The dissociation energy of this reaction, and of the endothermal loss of  $\text{Sb}_4$  from  $\text{Sb}_{12}^+$ ,  $\text{Sb}_{16}^+$ , and  $\text{Sb}_{20}^+$  as well, has been measured by electron impact ionization to be  $1.3 \pm 0.25 \text{ eV}^3$  (Table 2) Photodissociation experiments by Bréchignac and coworkers<sup>53</sup> support this value. They find an average dissociation energy for the loss of  $\text{Sb}_4$  from  $\text{Sb}_{4n}^+$  ( $n = 2$  to 20) of 1.35 eV.

The SID fragmentation patterns of the investigated  $\text{Sb}_n^+$  and  $\text{Bi}_n^+$  (up to eight atoms) are very similar (Fig. 5). Also, the decomposition of  $\text{Bi}_7^+$  and  $\text{Bi}_8^+$  is characterized by the preferred loss of neutral tetrameric (and dimeric) cluster units. This observation suggests that these cluster units, in particular the tetramer, might be major structural building blocks of the clusters of both semi-metals, as proposed from *ab initio* calculations for the antimony clusters.<sup>11</sup> Considering that the corresponding antimony and bismuth clusters are isoelectronic, it can be assumed that also in the case of the investigated bismuth cluster ions, the observed fragments are produced via the lowest energy unimolecular dissociation reactions. The larger abundance of smaller fragment ion signals observed already at lower collision energies in the SID spectra of bismuth clusters is explained by their generally lower binding energies than the corresponding antimony clusters (Table 1).

The fragmentation behavior of the cluster ions  $\text{Sb}_9^+$ ,  $\text{Sb}_{10}^+$ , and  $\text{Sb}_{11}^+$  has not been investigated previously. The decay of metastable  $\text{Sb}_{12}^+$  clusters after laser excitation has been shown to proceed as unimolecular decomposition reaction via the loss of  $\text{Sb}_4$  units as displayed in Fig. 5(a).<sup>53</sup> This is also the primary fragmentation reaction observed in our SID investigation for  $\text{Sb}_{12}^+$  and for the other cluster ions with nine to eleven atoms (Fig. 5(a)). Further major fragment ions of the clusters  $\text{Sb}_n^+$  ( $n = 9-12$ ) can be explained by the successive loss of neutral  $\text{Sb}_4$  and  $\text{Sb}_2$  units according to unimolecular fragmentation steps. This similar dissociation behavior for clusters belonging

to the series with a multiple of four atoms ( $\text{Sb}_8^+$  and  $\text{Sb}_{12}^+$ ) and those not belonging to this series ( $\text{Sb}_9^+$ ,  $\text{Sb}_{10}^+$  and  $\text{Sb}_{11}^+$ ) implies that there is no principal structural difference either between these clusters cations and that the tetrameric unit is an important structural unit. Further decomposition into smaller fragments is reduced, if one of the stable Wade-fragment ions  $\text{Sb}_5^+$  or  $\text{Sb}_7^+$  is formed.

If the vibrational energy, which is transferred to the fragment ion in the course of the collision process, is larger than its dissociation energy, and if competing dissociation pathways that require a comparable amount of energy are negligible, then a sequential decomposition takes place:



In Fig. 6 the fragment ion distributions of  $\text{Sb}_{10}^+$ ,  $\text{Sb}_{11}^+$  and  $\text{Sb}_{12}^+$  are displayed at three different collision energies. From these examples it can be seen that the intensities of the smaller fragments increase continuously with the collision energy which is characteristic for a sequential fragmentation reaction. In combination with the observed unimolecular fragmentation behavior, this observation will be used in the following section to determine energy conversion efficiencies during cluster-surface collision.

### C. Kinetic to internal cluster energy conversion upon collision

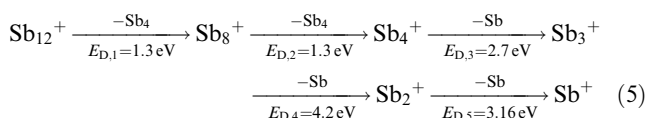
For a detailed understanding of the cluster surface interaction it is important to know the amount of the kinetic energy which is transferred into internal energy of the cluster in the course of the inelastic collision. The redistribution of the collision energy in surface phonon excitation, in thermal excitation of the colliding cluster as well as in the kinetic energy of the scattered cluster fragments cannot be observed directly in our experiment. However, if the decomposition mechanism proceeds *via* sequential dissociation reactions with similar entropy requirements and known reaction energies, it is possible to estimate the distribution of internal energies  $P(E)$  in a population of colliding cluster ions from the intensity patterns in the fragment ion mass spectra by applying simple thermochemical considerations.<sup>57</sup>

In the preceding discussion it could be shown that in the investigated range of hyperthermal collision energies, indeed a sequential fragmentation of the antimony clusters  $\text{Sb}_n^+$  ( $n \geq 7$ ) takes place with the preferred loss of stable neutral  $\text{Sb}_4$  and  $\text{Sb}_2$  units (Fig. 4). The reaction energies  $E_{D,i}$  for all the single unimolecular dissociation steps, however, are only known for  $\text{Sb}_8^+$  and  $\text{Sb}_{12}^+$ . The following reaction scheme (5) shows the successive fragmentation steps for  $\text{Sb}_{12}^+$  and

**Table 3** Appearance energies  $E_{a,i}$  of the fragments  $F_i^+$  and average internal energies  $E_i$  of the mother ion  $\text{Sb}_{12}^+$  according to the sequential dissociation reaction (5)

$i$	$F_i^+$	$E_{a,i}$ [eV]	$E_i$ [eV]
0	$\text{Sb}_{12}^+$	0	0.65
1	$\text{Sb}_8^+$	1.3	1.95
2	$\text{Sb}_4^+$	2.6	3.95
3	$\text{Sb}_3^+$	5.3	7.4
4	$\text{Sb}_2^+$	9.5	11.08
5	$\text{Sb}^+$	12.66	> 12.66

the corresponding dissociation energies (data are taken from references 31 and 3):



The method used here for the calculation of the internal energy distribution has been proposed by Cooks and coworkers.<sup>57,58</sup> Single values for the distribution of internal energies  $P(E_i)$  are deduced from the intensity of the fragment ions  $[F_i^+]$  weighted by the width of the energy interval  $[E_{a,(i+1)} - E_{a,i}]$  in which the fragment  $F_i^+$  is observed:

$$P_i(E_i) = \frac{[F_i^+]}{[E_{a,(i+1)} - E_{a,i}]} \quad (6)$$

$E_{a,i}$  is the energy at which the fragment  $F_i^+$  starts to appear, *i.e.* the minimum internal energy which the mother ion  $F_0^+$  needs in order to form such a fragment.  $E_i$  is the average internal energy that a mother ion  $F_0^+$  possessed which formed a fragment  $F_i^+$ . In Table 3 these values are listed for the fragmentation of  $\text{Sb}_{12}^+$  according to the reaction sequence (5).

Fig. 6(c) shows three fragment ion mass spectra of  $\text{Sb}_{12}^+$  obtained at collision energies of 30, 80 and 130 eV, respectively. The target surface is graphite. The distribution of internal energies  $P(E_i)$  obtained from the fragment ion intensities in these mass spectra in combination with the energy data in Table 3 are depicted in Fig. 7. Gaussian curves have been fitted to the data points, which reflect the distribution of internal energies at the different collision energies well as detailed, *e.g.*, in reference.<sup>49</sup> Characteristic for the SID compared to the other methods are the well defined impact parameters,

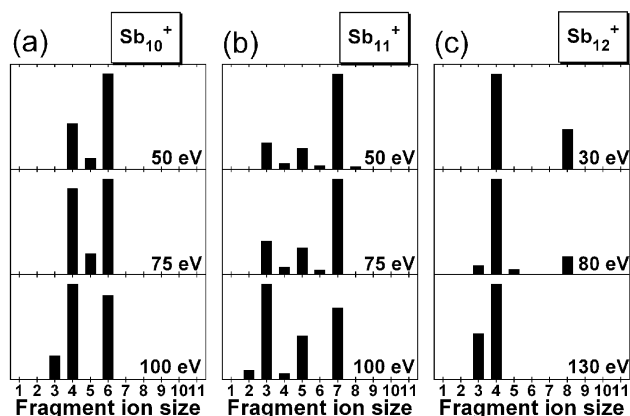


**Fig. 6** Fragment ion distributions of (a)  $\text{Sb}_{10}^+$ , (b)  $\text{Sb}_{11}^+$ , and (c)  $\text{Sb}_{12}^+$  measured at three different collision energies. Target surface: graphite.

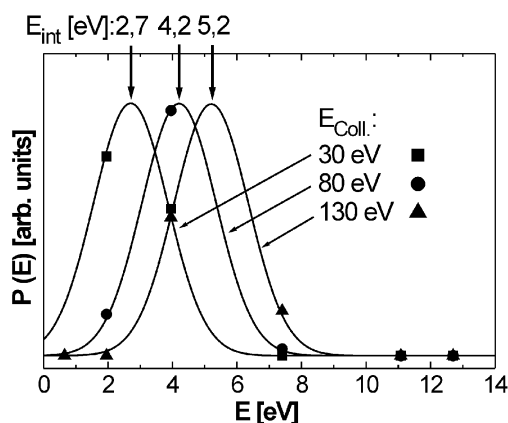


**Fig. 7** Internal energy distributions  $P(E)$  of  $\text{Sb}_{12}^+$  clusters at three collision energies calculated from the intensity distributions in Fig. 6 as explained in the text. Gaussian functions have been fitted to the data points at each collision energy which represent the estimated internal energy distribution. The average internal energies  $E_{\text{int}}$  are obtained from the maxima of the distributions.

the high energy conversion efficiency, and the relatively narrow distribution of internal energies that are deposited in the ion upon collision.<sup>48–50</sup> The maxima of the distribution curves give the average internal energy  $E_{\text{int}}$ , which is transferred to the cluster at the corresponding impact energy.  $E_{\text{int}}$  is plotted in Fig. 8 as a function of collision energy for the impact of  $\text{Sb}_{12}^+$  clusters onto graphite as well as onto a silicon surface. The energy transfer efficiency is largest (about 10%) at low collision energies and decreases almost linearly to about 4% at 150 eV collision energy. It is interesting to note that the amount of internal energy transferred to the cluster upon collision for the two different surfaces is comparable within about 1 eV although the target atomic mass and the elastic properties of the two surfaces are clearly different. It has been demonstrated theoretically quite recently that the energy transfer efficiency is, *e.g.*, a strong function of the surface stiffness.<sup>59</sup> Extended investigations of these issues with improved experimental energy resolution are in progress.<sup>60</sup>

Molecular dynamics simulations have shown the extreme thermodynamical conditions which are occurring for a very short time (on a femto- or picosecond time scale) during the cluster surface collision.<sup>61–64</sup> To relate the calculated internal energies to thermodynamical temperature values, we determine the vibrational temperatures  $T$  at the corresponding collision energies using the equipartitioning theorem

$$T = \frac{E_{\text{int}}}{(3n - 6)k_{\text{B}}}, \quad (7)$$

where  $k_{\text{B}}$  is the Boltzmann constant and  $(3n - 6)$  is the number of vibrational degrees of freedom in an  $n$  atom cluster. The thus obtained temperature scale is also included in Fig. 8. According to this estimation, vibrational temperatures of several thousand Kelvin can be achieved during the collision. Comparable temperatures have also been reported from MD-simulations of collisions of rare gas<sup>61–63</sup> and metal<sup>64</sup> clusters with solid surfaces. In a 200 eV collision of a  $\text{Cu}_{147}$  cluster with a Cu(111) surface, *e.g.*, temperatures up to 2100 K are present for several picoseconds.<sup>64</sup>

#### D. Scattered ion yield

The integral scattered ion yield in percent at a certain collision energy is obtained by integrating all fragment ion signals and normalizing this value to the total intensity of the colliding mother ion. The scattered ion yield is determined by the electronic interaction of the cluster ions with the surface, *i.e.* the neutralization process. The dependence of the integral scattered ion yield on the size of the colliding clusters thus gives

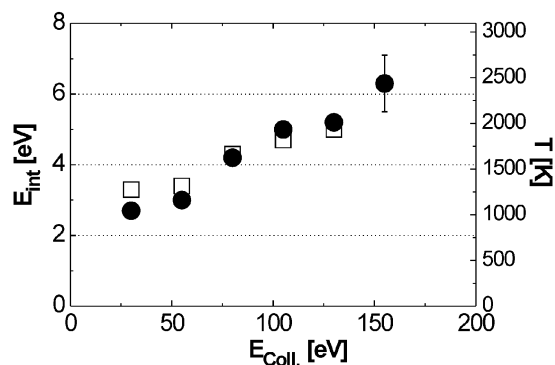


**Fig. 8** Average internal energies  $E_{\text{int}}$  acquired by an  $\text{Sb}_{12}^+$  cluster during collision with a graphite (filled circles) and a silicon surface (open squares) displayed as a function of collision energy, *i.e.* kinetic energy of the incident clusters. A typical error bar is shown. The right ordinate gives the vibrational temperatures at the corresponding internal energies calculated according to eqn. (7).

information about differences in the electronic structure of clusters with different number of atoms (for the same surface). In Fig. 9(a) and (b) the integral scattered ion yield of antimony clusters at a collision energy of 75 eV is displayed as a function of the size of the colliding mother ion. The results for the collision with a graphite and a silicon surface are shown. The overall trend for the antimony clusters is an increase in the scattered ion yield with increasing cluster size. However, this increase is not continuous. For both substrates and  $n > 5$ , larger scattered ion yields are measured for the scattering of clusters with an odd number of atoms in comparison to the adjacent cluster sizes with an even number of atoms.

Since the neutralization probability is a function of the energy difference between the ionization potential of the colliding cluster ion and the surface work function,<sup>47,50</sup> the observed higher average ion yield of the odd size clusters suggests that these clusters have in general lower ionization potentials than the even sized clusters. Up to now, however, there are no experimental or theoretical data available on the ionization potentials of  $\text{Sb}_n^+$  clusters with an odd number of atoms (for  $n \geq 5$ ). As discussed previously, the higher scattered ion yield for the silicon target can be related to its comparatively high work function, resulting in a weak neutralization efficiency.

The measured scattered ion yield for the  $\text{Bi}_n^+$  clusters scattering from graphite is larger than for the corresponding  $\text{Sb}_n^+$  clusters, which correlates well with the about 1 eV lower ionization potentials of bismuth clusters compared to antimony clusters.<sup>3</sup> The largest scattered ion yields for the graphite target, about 14% at 50 eV collision energy, have been measured for the odd size clusters  $\text{Bi}_5^+$  and  $\text{Bi}_7^+$ . The size variations are, however, within the experimental error bars. Also the known ionization potentials of bismuth clusters shows no marked variation in the size range between four and eight atoms.<sup>3–5</sup> Scattering bismuth clusters from the silicon target again leads to considerably enhanced scattered ion yields, as can be seen from Fig. 4(b) at, *e.g.*, 75 eV collision energy.

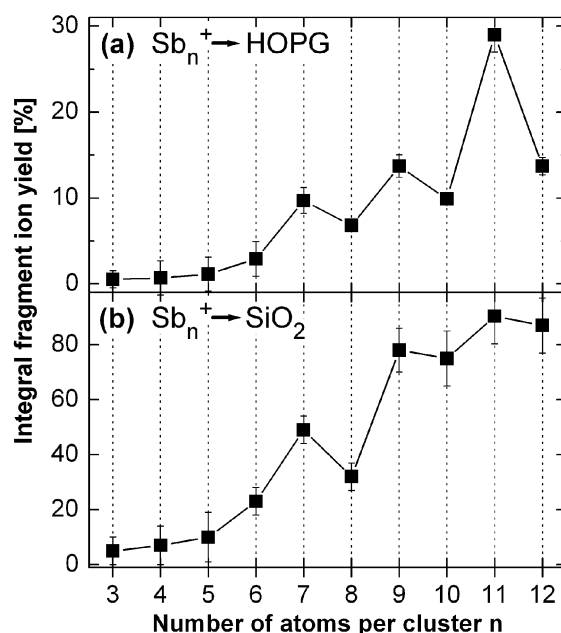


**Fig. 9** Integral scattered ion yield as a function of the size of the colliding cluster for the scattering of antimony clusters from different surfaces. (a)  $\text{Sb}_n^+$  scattered ion yield at a collision energy of 75 eV. Substrate: graphite. (b)  $\text{Sb}_n^+$  scattered from the silicon substrate (same impact energy). The error bars take into account the slightly different energy width in the different experiments as well as a larger error in the scattered ion yield at low collision energies due to the reflected mother cluster ions.



## IV. Conclusions

The fragmentation of semi-metal cluster ions of antimony and bismuth upon collision with a solid surface has been investigated. The decomposition of the cluster ions has been analyzed as a function of cluster size, collision energy, and surface type. By comparison with fragmentation data from the literature, it could be shown that in the investigated collision energy range up to 150 eV the clusters undergo a sequential unimolecular decomposition according to the lowest energy dissociation reactions. The fragment ion patterns of the investigated clusters and therefore the observed decomposition mechanism are found to be independent of the target surface. However, large changes in the overall scattered ion yield are observed for the different target surfaces employed. The highest scattered ion yield of up to 90% is detected for a high work function silicon oxide surface, whereas the scattering from a graphite and a metallic gold surface leads to considerably lower scattered ion yields. This is assigned to the difference in the electronic surface structure, in particular the surface work function. We also observe strong variations in integral scattered ion yield as a function of the cluster size for a given surface. The degree of conversion of kinetic energy to internal vibrational energy of the clusters was determined for  $\text{Sb}_{12}^+$  in collision with graphite and silicon surfaces. It varies between 4% at 130 eV and about 10% at 30 eV collision energy for both surfaces. The corresponding antimony and bismuth cluster ions show identical major fragment ions which points toward similar structural properties. Preferred loss of neutral tetramer and dimer units is observed. For the bismuth clusters smaller fragments are detected already at lower collision energies which reflects the lower stability of the bismuth cluster ions in comparison to antimony clusters.

## Acknowledgement

The work presented here has been supported by the Deutsche Forschungsgemeinschaft, the Fonds der Chemischen Industrie, and by the Humboldt Forschungsfonds.

## References

- 1 *Clusters of atoms and molecules*, ed. H. Haberland, Springer Ser. Chem. Phys., Springer, Berlin, vol. 52 and 56, 1994.
- 2 K. Sattler, J. Mühlbach and E. Recknagel, *Phys. Rev. Lett.*, 1980, **45**, 821.
- 3 D. Rayane, P. Melinon, B. Tribollet, B. Cabaud, A. Hoareau and M. Broyer, *J. Chem. Phys.*, 1989, **91**, 3100.
- 4 R. E. Walstedt and R. F. Bell, *Phys. Rev. A*, 1986, **33**, 2830.
- 5 R. E. Walstedt and R. F. Bell, *J. Chem. Phys.*, 1987, **87**, 1423.
- 6 J. Donohue, *The structures of the elements*, Wiley-Interscience, New York, 1974.
- 7 J. D. Corbett, *Prog. Inorg. Chem.*, 1976, **21**, 129.
- 8 J. D. Corbett, *Chem. Rev.*, 1985, **85**, 383.
- 9 K. Sattler, J. Mühlbach, P. Pfau and E. Recknagel, *Phys. Lett.*, 1982, **87A**, 418.
- 10 V. Kumar, *Phys. Rev. B*, 1993, **48**, 8470.
- 11 V. Sundararajan and V. Kumar, *J. Chem. Phys.*, 1995, **102**, 9631.
- 12 T. M. Bernhardt, B. Kaiser and K. Rademann, *Z. Phys. Chem.*, 1996, **195**, 273.
- 13 T. M. Bernhardt, B. Kaiser and K. Rademann, *Z. Phys. D*, 1997, **40**, 327.
- 14 B. Kaiser, T. M. Bernhardt, B. Stegemann, J. Opitz and K. Rademann, *Nucl. Instrum. Methods Phys. Res., Sect. B*, 1999, **157**, 155.
- 15 B. Kaiser, T. M. Bernhardt, B. Stegemann, J. Opitz and K. Rademann, *Phys. Rev. Lett.*, 1999, **83**, 2918.
- 16 *Cluster beam synthesis of nanostructured materials*, ed. P. Milani and S. Iannotta, Springer Series in Cluster Physics, Springer Verlag, Berlin, 1999.
- 17 *Metal clusters at surfaces*, ed. K.-H. Meiwes-Broer, Springer Series in Cluster Physics, Springer Verlag, Berlin, 2000.
- 18 B. Kaiser, T. M. Bernhardt and K. Rademann, *Nucl. Instrum. Methods Phys. Res., Sect. B*, 1997, **125**, 223.
- 19 J. Wönickhaus and J. A. Becker, *Rev. Sci. Instrum.*, 1994, **65**, 2019.
- 20 B. Kaiser, T. M. Bernhardt, M. Kinne, K. Rademann and A. Heidenreich, *J. Chem. Phys.*, 1999, **110**, 1437.
- 21 W. C. Wiley and I. H. McLaren, *Rev. Sci. Instrum.*, 1955, **26**, 1150.
- 22 B. A. Mamyrin, V. I. Karataev, D. V. Shmikk and V. A. Zagulin, *Sov. Phys. JETP (Engl. Transl.)*, 1973, **37**, 45.
- 23 B. A. Mamyrin and D. V. Shmikk, *Sov. Phys. JETP*, 1979, **49**, 762.
- 24 J. J. Metois, J. C. Heyraud and Y. Takeda, *Thin Solid Films*, 1978, **51**, 105.
- 25 J. A. DeRose, T. Thundat, L. A. Nagahara and S. M. Lindsay, *Surf. Sci.*, 1991, **256**, 102.
- 26 T. M. Bernhardt, B. Kaiser, and K. Rademann, to be published.
- 27 J. Mühlbach, P. Pfau, E. Recknagel and K. Sattler, *Surf. Sci.*, 1981, **106**, 18.
- 28 H. Sontag and R. Weber, *Chem. Phys.*, 1982, **70**, 23.
- 29 V. E. Bondybey, G. P. Schwartz and J. E. Griffiths, *J. Mol. Spectrosc.*, 1981, **89**, 328.
- 30 L.-S. Wang, B. Niu, Y. T. Lee, D. A. Shirley, E. Ghelichkhani and E. R. Grant, *J. Chem. Phys.*, 1990, **93**, 6318.
- 31 B. Cabaud, A. Hoareau, P. Nounou and R. Uzan, *Int. J. Mass Spectrom. Ion Phys.*, 1973, **11**, 157.
- 32 J. Kordis and K. A. Gingerich, *J. Chem. Phys.*, 1973, **58**, 5141.
- 33 G. M. Rosenblatt and P.-K. Lee, *J. Chem. Phys.*, 1970, **52**, 1454.
- 34 B. Stegemann, T. M. Bernhardt, B. Kaiser, and K. Rademann, *Surf. Sci.*, in press.
- 35 C. Bréchnignac, M. Broyer, P. Cahuzac, M. de Frutos, P. Labastie and J.-P. Roux, *Phys. Rev. Lett.*, 1991, **67**, 1222.
- 36 P. Pfau, K. Sattler, J. Mühlbach and E. Recknagel, *Phys. Lett.*, 1982, **91**, 316.
- 37 M. E. Geusic, R. R. Freeman and M. A. Duncan, *J. Chem. Phys.*, 1988, **89**, 223.
- 38 K. Wade, *Adv. Inorg. Chem. Radiochem.*, 1976, **18**, 1.
- 39 R. W. Rudolph, *Acc. Chem. Res.*, 1976, **9**, 446.
- 40 D. M. P. Mingos, T. Slee and L. Zhenyang, *Chem. Rev.*, 1990, **90**, 383.
- 41 R. B. King, *Inorg. Chim. Acta*, 1982, **57**, 79.
- 42 P. Fayet, M. J. McGlinchey and L. H. Wöste, *J. Am. Chem. Soc.*, 1987, **109**, 1733.
- 43 L. Rovner, A. Drowart and J. Drowart, *Transaction Faraday Soc.*, 1967, **63**, 2906.
- 44 E. Recknagel, *Ber. Bunsen-Ges. Phys. Chem.*, 1984, **88**, 201.
- 45 J. Mühlbach, P. Pfau, K. Sattler and E. Recknagel, *Z. Phys. B*, 1982, **47**, 233.
- 46 R. B. Gerber, *Chem. Rev.*, 1987, **87**, 29.
- 47 A. Amirav, *Comments At. Mol. Phys.*, 1990, **24**, 187.
- 48 R. G. Cooks, T. Ast and M. A. Mabud, *Int. J. Mass Spectrom. Ion Processes*, 1990, **100**, 209.
- 49 V. Grill, J. Shen, C. Evans and R. G. Cooks, *Rev. Sci. Instrum.*, 2001, **72**, 3149.
- 50 S. A. Miller, D. E. Riederer, Jr., R. G. Cooks, W. R. Cho, H. W. Lee and H. Kang, *J. Phys. Chem.*, 1994, **98**, 245.
- 51 R. D. Beck, C. Warth, K. May and M. M. Kappes, *Chem. Phys. Lett.*, 1996, **257**, 557.
- 52 M. M. Ross and S. W. McElvany, *J. Chem. Phys.*, 1988, **89**, 4821.
- 53 C. Bréchnignac, P. Cahuzac, F. Carlier, M. de Frutos, J. Leygnier and J.-P. Roux, *J. Chem. Phys.*, 1995, **102**, 763.
- 54 M. E. Geusic, R. R. Freeman and M. A. Duncan, *J. Chem. Phys.*, 1988, **88**, 163.
- 55 R. K. Yoo, B. Ruscic and J. Berkowitz, *J. Chem. Phys.*, 1992, **96**, 6696.
- 56 *Handbook of Chemistry and Physics*, ed. D. R. Lide, CRC Press, Boca Raton, 1995.
- 57 H. I. Kenttämaa and R. G. Cooks, *Int. J. Mass Spectrom. Ion Processes*, 1985, **64**, 79.
- 58 M. J. DeKrey, H. I. Kenttämaa, V. H. Wysocki and R. G. Cooks, *Org. Mass Spectrom.*, 1986, **21**, 193.
- 59 O. Meroueh and W. L. Hase, *Phys. Chem. Chem. Phys.*, 2001, **3**, 2306.
- 60 J. Opitz-Coutureau and B. Kaiser, to be published.
- 61 C. L. Cleveland and U. Landmann, *Science*, 1992, **257**, 355.
- 62 U. Even, I. Schek and J. Jortner, *Chem. Phys. Lett.*, 1993, **202**, 303.
- 63 I. Schek and J. Jortner, *J. Chem. Phys.*, 1996, **104**, 4337.
- 64 H.-P. Cheng and U. Landmann, *J. Phys. Chem.*, 1994, **98**, 3527.
- 65 F. J. Kohl, O. M. Uy and K. D. Carlson, *J. Chem. Phys.*, 1967, **47**, 2667.
- 66 T. M. Bernhardt, *PhD Thesis*, Humboldt-University, Berlin, 1997.